

Exploring modulation instability, PINN-predicted solutions, and dynamic behavior of the Hirota equation

Muchen Li(李沐辰), Yaqing Liu(刘亚轻), Yuwen Han(韩钰文)
Citation: Chin. Phys. B. 35, 090203 (2026). DOI: 10.1088/1674-1056/ae8003 | CSTR: 32038.14.CPB.ae8003
http://cpb.iphy.ac.cn; http://iopscience.iop.org/cpb

What follows is a list of articles you may be interested in

Soliton collision, modulation instability and long-time asymptotic for non-autonomous solutions in the variable-coefficient coupled Schrödinger-KdV equations

Tongshan Liu(刘桐杉), Li Li(李丽), Fajun Yu(于发军)
Chin. Phys. B. 35, 090201 (2026). DOI: 10.1088/1674-1056/ae60ed | CSTR: 32038.14.CPB.ae60ed

The N-soliton solutions of the three-component coupled nonlinear Hirota equations based on Riemann–Hilbert method

Xin Wang(王昕), Zhi-Hui Zhang(张智辉)
Chin. Phys. B. 34, 090202 (2025). DOI: 10.1088/1674-1056/adce9c | CSTR: 32038.14.CPB.adce9c

Multi-soliton solutions, breather-like and bound-state solitons for complex modified Korteweg–de Vries equation in optical fibers

Zhong-Zhou Lan(兰中周)
Chin. Phys. B. 33, 060201 (2024). DOI: 10.1088/1674-1056/ad39d7

Nondegenerate solitons of the (2+1)-dimensional coupled nonlinear Schrödinger equations with variable coefficients in nonlinear optical fibers

Wei Yang(杨薇), Xueping Cheng(程雪苹), Guiming Jin(金桂鸣), Jianan Wang(王佳楠)
Chin. Phys. B. 32, 120202 (2023). DOI: 10.1088/1674-1056/acf282

Trajectory equation of a lump before and after collision with other waves for generalized Hirota–Satsuma–Ito equation

Yarong Xia(夏亚荣), Kaikai Zhang(张开开), Ruoxia Yao(姚若侠), Yali Shen(申亚丽)
Chin. Phys. B. 32, 100201 (2023). DOI: 10.1088/1674-1056/acd62c

---

SPECIAL TOPIC — Nonlinear localized waves: Theory, methods and applications

Exploring modulation instability, PINN-predicted solutions, and dynamic behavior of the Hirota equation

Muchen Li(李沐辰), Yaqing Liu(刘亚轻)†, and Yuwen Han(韩钰文)

School of Applied Science, Beijing Information Science and Technology University, Beijing 100192, *China*

(Received 17 May 2026; revised manuscript received 14 June 2026; accepted manuscript online 22 June 2026)

The Hirota equation serves as a significant integrable mathematical model for nonlinear phenomena, and its study is of great significance in fields such as nonlinear optics and fluid dynamics. In this paper, we numerically solve the Hirota equation using a physics-informed neural network (PINN) and conduct a modulation instability analysis, successfully determining the parameter range of unstable waves and providing a theoretical basis for the existence of rogue waves. PINN embeds the governing equations as soft constraints directly into the neural network and minimizes the loss function to enable the PINN model to learn solutions that conform to physical laws from limited training data. In this study, the one-, two-, and three-soliton solutions as well as the first- and second-order rogue wave solutions of the Hirota equation are successfully simulated using PINN. The PINN model exhibits high accuracy in predicting the complex dynamics of the Hirota equation, and the predicted waveforms and propagation characteristics are highly consistent with the corresponding exact analytical solutions. The numerical solutions obtained using PINN provide a new approach for analyzing and solving equations with complex interactions or general initial and boundary conditions. This study confirms that PINN, as a data-efficient and meshless computational tool, can be utilized to compute numerical solutions of nonlinear partial differential equations and investigate the dynamic structures inherent in complex nonlinear equations, providing a highly promising computational method for numerical research in nonlinear science.

Keywords: Hirota equation, physical-informed neural network model, modulation instability, soliton solutions, Rogue wave solution

PACS: 02.30.Ik, 02.60.Cb, 05.45.Yv, 07.05.Mh

DOI: 10.1088/1674-1056/ae8003 **CSTR:** 32038.14.CPB.ae8003

1. Introduction

Nonlinear partial differential equations (PDEs) serve as the fundamental mathematical framework for describing complex phenomena in fields such as science and engineering, ranging from the complex dynamics of fluid flow and plasma physics to the propagation of light signals in optical fibers and the fundamental interactions in quantum field theory. These equations reflect the relationships that exist in nonlinear dynamic evolution processes. Localized waves are an important type of solution to PDEs, and they can maintain their shape and energy over long distances. Solitons and rogue waves are two typical examples of localized structures. In completely integrable systems, solitary waves possess extremely high stability and are wave packets resembling particles, formed by the delicate balance between nonlinearity and dispersion. They can propagate without changing their shape and can be perfectly reproduced after a collision. This characteristic makes solitary waves a powerful model for energy transmission in fields such as optics.[1,2] In addition, solitons may also generate soliton molecules[3] and soliton interactions[4–9] during their motion or collision. In contrast, rogue waves[10,11] are rare, high-amplitude events that seemingly appear out of nowhere and then disappear without a trace. These 'devastating waves' were initially observed as huge ocean waves but were later identified in various systems such as nonlinear optics, Bose-Einstein condensates, and even financial markets.

At present, research on PDEs has made certain progress in analytical theory and numerical methods, including the Darboux transform,[12] scattering transform,[13,14] Bäcklund transform,[15] Hirota bilinear method,[16,17] Riemann-Hilbert method,[18] and other auxiliary computational tools.[19–22] However, these methods are usually only applicable to partially integrable systems, specific boundary conditions, and relatively simple solution structures. Highly nonlinear, multi-scale, or high-dimensional PDEs still face many challenges. The Hirota bilinear method has difficulties in handling derivative terms and non-zero boundary conditions, while the inverse scattering transform process is complex and requires strict initial values.[23] These limitations make traditional methods difficult to apply to more general initial and boundary value conditions, non-integrable variations, complex interacting solutions, and higher-dimensional extensions. Therefore, these challenges have promoted the development of numerical solution methods, and some related methods have been proven to have good solution performance, such as the finite volume

†Corresponding author. E-mail: liuyaqing@bistu.edu.cn

© 2026 Chinese Physical Society and IOP Publishing Ltd. All rights, including for text and data mining, AI training, and similar technologies, are reserved.

method (FVM),[24] finite difference method (FDM),[25] and finite element method (FEM).[26] However, these numerical methods cannot avoid the complexity of mathematical analysis and the high computational cost of numerical simulations. These limitations have prompted researchers to explore new solution paradigms, which has driven the development of advanced theories and computational tools.

In recent years, machine learning has become an important method for solving PDE problems. One promising development is the PINN.[27] Deep neural networks are utilized in PINN to approximate partial differential equation solutions, a strategy that involves embedding physical laws alongside boundary conditions directly into the network's loss function. Required derivatives undergo efficient calculation via the mechanism of automatic differentiation (AD). This approach makes PINN inherently mesh-free, highly flexible for both forward and inverse problems,[28] and very efficient in data utilization. The powerful capabilities of PINN have significant applications in fields such as fluid dynamics, heat transfer, power systems, and battery modeling.[29–31] Current PINN research is mainly divided into three research directions: applying PINN to different types of PDEs; improving the training methods and model architectures of PINN; and enhancing the solution accuracy for specific equations by introducing specific mathematical methods from the relevant fields.

PINN has currently been successfully applied to solve various classical and complex PDEs. Pu *et al.*[32] used the optimized PINN model to simulate the localized wave solutions of the nonlinear Schrödinger equation (NLSE); Han *et al.*[33] applied the PINN method to the Gerdjikov-Ivanov (GI) equation and successfully reproduced the soliton solutions and rogue wave solutions of this equation. Regarding the improvement of the PINN model, relevant researchers have proposed various variants of PINN to improve the training stability, accuracy, and generalization ability of PINN. Yu *et al.*[34] proposed the gradient-enhanced PINN (gPINN), which improves the stability and generalization ability of the neural network by adding additional gradient terms to the loss function; Yuan *et al.*[35] proposed the adaptive activation function (APINN) to obtain more accurate solutions for PDEs; Zhou *et al.*[36] proposed a residual-based adaptive multi-distribution (RAMD) sampling method, which optimizes the PINN training process by dynamically constructing a multi-modal loss distribution, thereby boosting accuracy while reducing complexity and stabilizing gradients. As for research on obtaining better solutions by adding relevant mathematical methods, the characteristics of the respective equations are often utilized to adjust PINN. Lax pair-guided neural networks (LPNNs) are obtained for solving the KdV equation by combining the Lax pair with PINN in integrable systems,[37] while the Darboux transformation-based LPNN (DT-LPNN) is utilized to investigate the Kaup–Mikhailov–Manakov system.[38]

The study of the dynamics of nonlinear systems often begins with the standard NLSE. Following the normalization used in many fundamental studies, the dimensionless form of the NLSE can be written as

$$\mathrm{i}q_t + q_{xx} + 2|q|^2 q = 0, \tag{1}$$

where x and t are independent variables, q is a complex-valued solution that captures the interaction between two fundamental effects: group velocity dispersion (q_{xx}) and self-phase modulation ($2|q|^2 q$). The imaginary unit i is defined by the property that $\mathrm{i}^2 = -1$.

However, in the field of optics, the effectiveness of the NLSE mainly depends on the pulse duration and intensity. As laser technology enters the femtosecond domain, higher-order effects such as third-order dispersion become significant and cannot be ignored for such ultrashort pulses. This has led to the emergence of various extended NLSE models, which require the inclusion of higher-order terms in the Taylor expansion of the propagation constant and the nonlinear response function. This has resulted in the formation of the generalized high-order NLSE. This form was initially proposed by Kodama and Hasegawa[39]

$$\mathrm{i}q_t + \frac{1}{2}q_{xx} + q|q|^2 + \mathrm{i}c_1 q_{xxx} + c_2 q\left(|q|^2\right)_x + \mathrm{i}c_3\left(q|q|^2\right)_x = 0, \tag{2}$$

where the coefficients c_1, c_2, and c_3 are real constants used to weight the corresponding higher-order physical effects. $\mathrm{i}c_1 q_{xxx}$ is the third-order dispersion, while $c_2 q(|q|^2)_x$ and $\mathrm{i}c_3(q|q|^2)_x$ are responsible for the nonlinear effects beyond the instantaneous Kerr response.

The general high-order nonlinear Schrödinger equation (HNLSE) is usually non-integrable, but when there is a specific relationship among the coefficients of the higher-order terms, the HNLSE can maintain the property of complete integrability. Extensive research has identified several such integrable high-order NLSEs. Whether these equations are integrable depends on the proportional relationship among these three higher-order coefficients $c_1 : c_3 : \mathrm{Im}(c_2) + c_3$. Among these integrable equations, several important integrable equations have emerged, including the Hirota equation, the Sasa-Satsuma equation, and some variations of the generalized NLSE.[40,41]

The Hirota equation is a very important type of equation in the integrable case of the HNLSE. It precisely balances the third-order dispersion and the time-delay correction of the third-order nonlinear term, thereby maintaining the integrability of the equation and providing a more accurate description of wave propagation and related dynamical behaviors.[42] Its complete integrability implies the existence of exact solutions,

including solitary waves, breathing waves, and rogue waves, making it an ideal theoretical laboratory for studying complex nonlinear dynamics. By setting the coefficients in the generalized HNLSE (2) such that their proportional relationship is $c_1 : c_3 : \mathrm{Im}(c_2) + c_3 = 1/2 : 3 : 0$, when $c_1 = 1/2$, $c_2 = -3\mathrm{i}$ and $c_3 = 3$ in the HNLSE (2), it transforms into the following form:

$$\mathrm{i}q_t + \frac{1}{2}q_{xx} + q|q|^2 + \frac{1}{2}\mathrm{i}q_{xxx} + 3\mathrm{i}|q|^2 q_x = 0, \tag{3}$$

where another equivalent form of the Hirota equation is as follows:

$$\mathrm{i}q_t + \alpha(q_{xx} + 2|q|^2 q) + \mathrm{i}\beta\left(q_{xxx} + 6|q|^2 q_x\right) = 0, \tag{4}$$

where α controls the relative strengths of the group velocity dispersion and Kerr nonlinearity, while β controls the higher-order effects of third-order dispersion and self-steepening. When $\alpha = 1/2$ and $\beta = 1/2$, this equation is equivalent to Eq. (3); when $\alpha = 0$, this equation reduces to the complex modified KdV equation; when $\beta = 0$, the equation reduces to the standard NLSE (1).

At present, for the Hirota equation with high-order dispersion and nonlinear terms, there is no unified PINN framework used to completely solve the multi-soliton solutions and multi-order rogue wave solutions of the Hirota equation and conduct a systematic study of their dynamic behaviors. The numerical prediction of solutions and dynamic simulations of the Hirota equation are still insufficient. Therefore, by leveraging the powerful fitting ability and physical constraint characteristics of PINN, systematically studying the localized wave solutions of the Hirota equation can not only fill the research gap in the field of scientific machine learning for this equation, but also provide new theoretical tools and simulation methods for applications such as pulse control in optical communication and the prediction of extreme wave events.

The remainder of this paper is organized as follows. Section 2 presents the PINN framework. Section 3 presents the modulation instability analysis. Sections 4 and 5 respectively present the numerical results of the N-soliton solutions and the rogue solutions. Finally, Section 6 summarizes our findings and concludes the paper.

2. Physics-informed neural network

The PINN has certain advantages over traditional numerical methods in solving partial differential equation problems. PINN is naturally suitable for complex geometric regions and non-standard boundary conditions without the need to generate grids. It can simultaneously solve for the unknown solution and determine the equation parameters, providing assistance for inverse problem research.[43] It demonstrates strong scalability and cross-domain generalization capabilities.[44] The PINN model is capable of achieving high-precision solutions even when the available training samples are limited in number.[45] Once the network is trained, the solution value at any point within the domain can be quickly obtained, and similar problem-solving tasks can be accelerated through transfer learning.

Figure 1 conceptually presents the architecture of the PINN framework we use to solve nonlinear PDEs such as the Hirota equation. Specifically, the basic principle of PINN is to combine fundamental physical laws with deep learning.[46] It constructs a framework that combines the deep learning model with physical laws. This framework consists of three core modules: the neural network, automatic differentiation (AD), and the loss function. The neural network (Fig. 1, left side) is used as a general function approximator to represent the solution of a given equation, while a specially designed loss function requires alignment between model outputs and fundamental physical principles. It takes the spatial and temporal coordinates (x,t) as input, processes them through multiple fully connected hidden layers with activation functions, and outputs the real part $u(x,t)$ and the imaginary part $v(x,t)$ of the complex solution $q(x,t) = u(x,t) + \mathrm{i}v(x,t)$. This objective is realized by transforming physical constraints, which encompass the partial differential equation itself alongside its initial and boundary conditions, into mathematical penalty terms and subsequently embedding them within the training process of the neural network. Throughout the training process, the model not only minimizes the discrepancy between its predicted values and any available observational data, but is also compelled to satisfy the partial differential equation. This dual-objective optimization balances the data-driven and physics-driven aspects of the problem, resulting in a solution that accurately conforms to physical laws.[47] In this study, the random seeds used for sampling were all set to "seed = 1234". The outputs u and v of the neural network are then input into the AD module (Fig. 1, center section), where the AD module can accurately and efficiently calculate the derivatives required for computing the PDE residual, thereby avoiding the inherent discretization errors in traditional numerical methods.

After the AD section, these calculated derivative terms and the original outputs continue to enter the loss function module (Fig. 1, right side), forming a composite loss function $\psi(\theta)$. The total loss function calculated during the training process is composed of the weighted sum of two different parts: one is the term related to the initial and boundary data, and the other is the term related to the residual of the physical equation. The total loss ψ can be expressed as

$$\psi(\theta) = w_{\mathrm{data}}\psi_{\mathrm{data}} + w_{\mathrm{phy}}\psi_{\mathrm{phy}}, \tag{5}$$

where θ represents the set of all trainable parameters (weights and biases) in the neural network, ψ_{data} is the data loss term,

ψ_{phy} is the physical loss term, and w_{data} and w_{phy} are hyperparameters used to balance the weights corresponding to each loss, thereby preventing one loss term from dominating to the extent that it affects the convergence of the training process.[48,49]

This study utilized the PINN framework to solve the complex-valued solutions $q(x,t)$ of the Hirota equation (Eq. (4)) with high efficiency. We set the values of this analytical solution at the initial time $t = t_{\min}$ and at the boundaries $x = x_{\min}$ and $x = x_{\max}$ as Dirichlet conditions for constraint. We used the Latin hypercube sampling method to generate interpolation points so as to achieve uniform and comprehensive coverage of the entire spatiotemporal solution space. To apply the PINN framework to the Hirota equation, we decompose the complex solution $q(x,t)$ into its real and imaginary parts, $q(x,t) = u(x,t) + \mathrm{i}v(x,t)$, where $u(x,t)$ and $v(x,t)$ are real-valued functions. Substituting this into the Hirota equation and separating the real and imaginary components yields a system of two coupled equations

$$\begin{aligned} f_u &:= -v_t + \alpha[u_{xx} + 2u(u^2+v^2)] \\ &\quad -\beta[v_{xxx} + 6(u^2+v^2)v_x] = 0, \\ f_v &:= u_t + \alpha[v_{xx} + 2v(u^2+v^2)] \\ &\quad +\beta[u_{xxx} + 6(u^2+v^2)u_x] = 0, \end{aligned} \tag{6}$$

where the equations f_u and f_v represent the physical constraints that the solution of the neural network must satisfy.

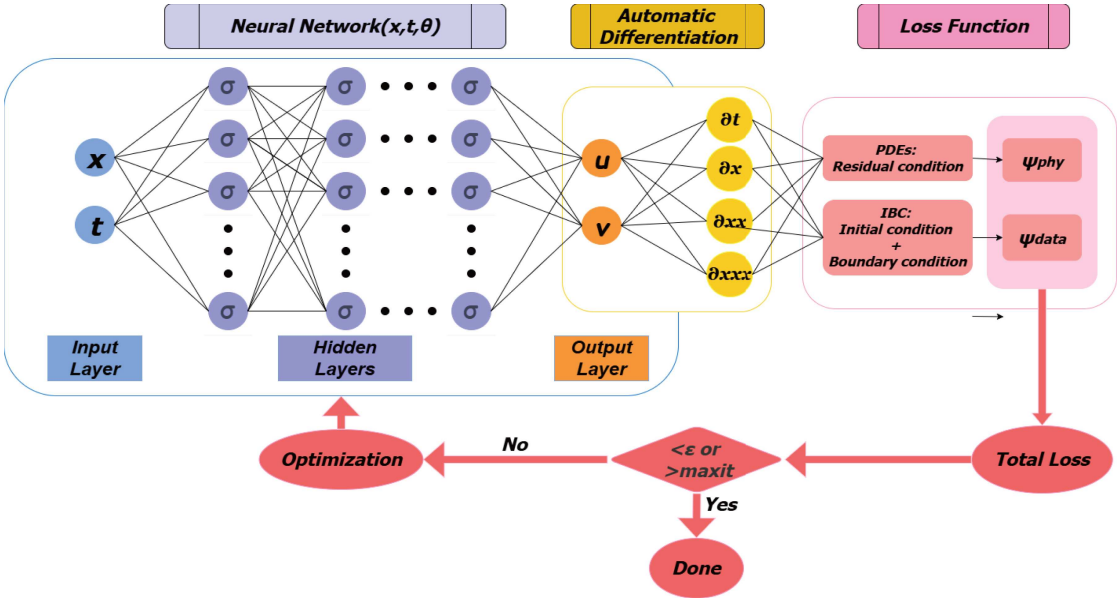


Fig. 1. Schematic diagram of the PINN.

The data loss ψ_{data} is used to measure the difference between the network's predicted results and the known initial and boundary conditions of the system. Usually, it is defined as the mean square error of N_{data} points sampled at the initial time and at the boundary of the region

$$\psi_{\text{data}} = \frac{1}{N_{\text{data}}} \sum_{i=1}^{N_{\text{data}}} \left[(u(x_u^i, t_u^i) - u^i)^2 + (v(x_v^i, t_v^i) - v^i)^2 \right], \tag{7}$$

where the data loss ψ_{data} is composed of the predicted values $u(x,t)$ and $v(x,t)$, as well as the corresponding true values u^i and v^i. This implies that the initial and boundary conditions of $q(x,t)$ are provided by the datasets $\{x_u^i, t_u^i, u^i\}$ and $\{x_v^i, t_v^i, v^i\}$.

The physical loss term ψ_{phy} drives the learned solution to satisfy the Hirota equation throughout the entire spacetime domain. It is calculated by using the Latin hypercube sampling method to extract N_{phy} sampling points and evaluating the mean square error of the partial differential equation residuals f_u and f_v

$$\psi_{\text{phy}} = \frac{1}{N_{\text{phy}}} \sum_{j=1}^{N_{\text{phy}}} \left[f_u(x_{f_u}^j, t_{f_u}^j)^2 + f_v(x_{f_v}^j, t_{f_v}^j)^2 \right], \tag{8}$$

where the physics loss ψ_{phy} forces the solution of the neural network to conform to the physical constraints defined by Eq. (6). The collocation points for f_u and f_v are specified by $\{x_{f_u}^j, t_{f_u}^j\}$ and $\{x_{f_v}^j, t_{f_v}^j\}$.

The network is trained by iteratively adjusting its weights and biases to minimize this total loss function (the bottom of Fig. 1). The total loss $\psi(\theta)$ guides an optimizer that calculates gradients, updates parameters θ, and feeds them back to the network. This iterative forward-backward process continues until convergence (loss $< \varepsilon$ or iteration count $>$ maxit), ensuring that the obtained solution both meets the data requirements and conforms to physical laws. Regarding the neural network structure, a multi-layer perceptron (MLP) is utilized, with weights initialized via Xavier (Glorot) initializa-

tion to drive a stable distribution of activation values across each layer. For reproducibility, we detail our model's hyperparameters. The network architecture consists of 4 to 5 hidden layers with 20 to 100 neurons each. The number of initial boundary points N_u was selected as $\{200, 300\}$, and the number of collocation points N_f was selected as $\{10000, 15000\}$. The loss weights w_{data} and w_{phy} were tested in $\{0.5, 1, 2\}$ to adjust these weights when the sampling of collocation points is severely imbalanced, thereby improving the overall residuals. Within the scope of this study, it was observed that the relative L_2 error did not change significantly within a reasonable time and space range and with an appropriate learning rate. This indicates that this method is robust to moderate perturbations of the hyperparameters. Therefore, in the experiments reported here, the loss weights can be set such that the ratio of w_{data} to w_{phy} is 1:1. The hyperbolic tangent (tanh) activation function is used due to its smoothness and suitability for approximating solutions of PDEs that require high-order derivatives.

The training process of this PINN aims to find the optimal set of network parameters θ^* that minimizes the total loss function $\psi(\theta)$, which is a very challenging nonlinear optimization problem. A common and effective method is to use the limited-memory Broyden–Fletcher–Goldfarb–Shanno (L-BFGS) algorithm, which is a quasi-Newton method suitable for full-batch gradient optimization.[50] L-BFGS improves the optimization steps by approximating the inverse Hessian matrix. This optimization method can achieve convergence faster and yield more accurate results than ordinary first-order methods. It also performs well in the final stage of training.

This PINN architecture can leverage the function approximation capability of deep neural networks while adhering to the underlying physical laws. It is suitable for solving nonlinear wave dynamics problems with multi-scale features and complex interactions. Currently, it has become a highly promising numerical computing tool and has broad application prospects in numerous fields of computational science and engineering.

3. Modulation instability of the Hirota equation

Modulation instability (MI)[51] is a common fundamental phenomenon in nonlinear science. It is a basic mechanism that describes the interplay between nonlinearity and dispersion in a system and the resulting instability. This process occurs in a nonlinear medium with a plane-wave background, which becomes unstable under small perturbations. Under the condition of modulation instability, these perturbations undergo exponential growth rather than decay. This growth can serve as a precursor to various dynamical structural changes.[52] Under the condition of modulation stability, these small perturbations oscillate and decay, allowing the system to maintain a uniform state. Therefore, conducting a modulation instability analysis to determine the parameter regions of instability is a key prerequisite for understanding the rogue-wave phenomena that may occur in systems governed by the Hirota equation.

This section investigates the baseband MI of the wave solutions of the Hirota equation (4). We consider a plane-wave solution of the Hirota equation, which serves as the basis for the subsequent perturbation analysis. The form of this plane-wave solution is

$$q_0(x,t) = A\,\mathrm{e}^{\mathrm{i}(kx-\omega t)}, \tag{9}$$

where A represents the amplitude of the wave, k is the wavenumber, and ω is the frequency. These parameters are interconnected through the dynamical relations of the nonlinear system. By substituting Eq. (9) into the Hirota equation (4), the nonlinear dispersion relation can be derived

$$\omega = 6A^2\beta k - \beta k^3 - 2A^2\alpha + \alpha k^2. \tag{10}$$

The core of the MI analysis lies in verifying the stability of this plane-wave solution q_0 under small perturbations. Therefore, we introduce a small perturbation $\varepsilon p(x,t)$, where $\varepsilon \ll 1$, to the amplitude of the plane-wave solution. The perturbation $p(x,t)$ is a general periodic function, which can be expressed as a linear combination of complex exponential functions with specific frequencies and wavenumbers. The perturbed wave can thus be written as

$$q(x,t) = (A + \varepsilon p(x,t))\,\mathrm{e}^{\mathrm{i}(kx-\omega t)}, \tag{11}$$

$$p(x,t) = \mu\,\mathrm{e}^{\mathrm{i}(Kx-\Omega t)} + \nu\,\mathrm{e}^{-\mathrm{i}(Kx-\Omega t)}, \tag{12}$$

where μ and ν are the amplitudes of the two wavenumber and frequency components. In this analysis, we employ a perturbation term $p(x,t)$ with wavenumber K and frequency Ω, representing it as a superposition of forward- and backward-propagating sidebands.

Based on Euler's formula $\mathrm{e}^{\mathrm{i}x} = \cos x + \mathrm{i}\sin x$, the imaginary part of the exponential function can be expressed in terms of trigonometric functions, resulting in an oscillatory form that does not lead to exponential growth. However, if the imaginary part of Ω is nonzero, then $\mathrm{i}\Omega$ acquires a real component, and the perturbation p exhibits exponential growth. Consequently, q also exhibits exponential growth. Therefore, the goal is to determine the conditions under which Ω becomes complex.

We proceed by substituting the perturbed solution $q(x,t)$ into the Hirota equation (4). This results in a complex equation containing terms of different orders in (ε. First, for the zeroth-order term in ε (ε^0), since $q(x,t) = q_0(x,t)$ and the unperturbed solution q_0 already satisfies the Hirota equation, the zeroth-order terms cancel due to the dispersion relation. Second, the higher-order terms in ε (ε^2 and ε^3) can be neglected because $\varepsilon \ll 1$. Therefore, only the linear term in ε is retained

for the subsequent perturbation analysis. The resulting expression is

$$\begin{aligned}\boldsymbol{H}(\varepsilon) = &\left\{2\left\{A^2(-3\beta k+\alpha)\mu\right.\right.\\&+2\nu\left\{\left[\left(\frac{3K}{2}-3k\right)A^2-\frac{(K-k)^3}{4}\right]\beta\right.\\&\left.\left.+A^2\alpha-\frac{\alpha K^2}{4}+\frac{\alpha Kk}{2}-\frac{\alpha k^2}{4}+\frac{\omega}{4}-\frac{\Omega}{4}\right\}\right\}\\&\times \mathrm{e}^{\mathrm{i}(\Omega-\omega)t-\mathrm{i}(K-k)x}\\&+4\left\{\left\{\left[\left(-\frac{3K}{2}-3k\right)A^2+\frac{(K+k)^3}{4}\right]\beta\right.\right.\\&\left.+A^2\alpha-\frac{\alpha K^2}{4}-\frac{\alpha Kk}{2}-\frac{\alpha k^2}{4}+\frac{\omega}{4}+\frac{\Omega}{4}\right\}\mu\\&\left.+\frac{A^2\nu(-3\beta k+\alpha)}{2}\right\}\mathrm{e}^{-\mathrm{i}(\Omega+\omega)t+\mathrm{i}(K+k)x}\Big\}\varepsilon. \quad (13)\end{aligned}$$

This process yields a set of coupled linear algebraic equations for the sideband amplitudes μ and ν. After substituting ω from Eq. (10) and separating the terms corresponding to the $\mathrm{e}^{\mathrm{i}(kx-\omega t)}\mathrm{e}^{\mathrm{i}(Kx-\Omega t)}$ and $\mathrm{e}^{\mathrm{i}(kx-\omega t)}\mathrm{e}^{-\mathrm{i}(Kx-\Omega t)}$ modes, we obtain a homogeneous system of two linear equations. This system can be expressed in matrix form

$$\begin{pmatrix}M_{11} & M_{12}\, M_{21} & M_{22}\end{pmatrix}\begin{pmatrix}\mu & \nu\end{pmatrix} = 0, \quad (14)$$

where

$$\begin{aligned}M_{11} &= -\varepsilon\left(6\beta KA^2+6\beta kA^2-\beta K^3-3\beta K^2k-3\beta Kk^2\right.\\&\quad\left.-2A^2\alpha+\alpha K^2+2\alpha Kk-\Omega\right),\\M_{12} &= -6\varepsilon A^2\left(\beta k-\frac{\alpha}{3}\right),\\M_{21} &= -6\varepsilon A^2\left(\beta k-\frac{\alpha}{3}\right),\\M_{22} &= \varepsilon\left(6\beta KA^2-6\beta kA^2-\beta K^3+3\beta K^2k-3\beta Kk^2\right.\\&\quad\left.+2A^2\alpha-\alpha K^2+2\alpha Kk-\Omega\right).\end{aligned}$$

The elements of the matrix $\boldsymbol{M}$ are intricate functions of the background parameters A and k, the perturbation parameters K and Ω, and the coefficients of the Hirota equation. For this system to have a nontrivial solution for μ and ν, the determinant of the coefficient matrix must be zero. This condition, $\det(M)=0$, provides the dispersion relation for the perturbation, which links its frequency Ω to its wavenumber K.

After a detailed calculation, the frequency of the perturbation Ω is found to be related to its wavenumber K by the following expression:

$$\begin{aligned}\Omega &= 6A^2\beta K-K^3\beta-3\beta k^2K+2\alpha kK\\&\quad\pm\sqrt{-K^2(\alpha-3\beta k)^2(4A^2-K^2)}. \quad (15)\end{aligned}$$

The rate of exponential growth is quantified by the MI gain G, which is defined as the magnitude of the imaginary part of Ω. The gain is given by

$$G = |\mathrm{Im}(\Omega)| = \left|\sqrt{-K^2(\alpha-3\beta k)^2(4A^2-K^2)}\right|. \quad (16)$$

This relation is the central result of the linear stability analysis. When the amplitude of the disturbance p increases exponentially with time, MI occurs. This occurs if Ω has a nonzero imaginary part. From Eq. (15), this is possible only when the argument of the square root is negative, and the crucial dynamics are contained in the square-root term. Since $K^2(\alpha-3\beta k)^2$ is always nonnegative, the condition for instability becomes $K^2-4A^2<0$, that is, $|K|<|2A|$.

Figure 2 presents the key results of the MI analysis for the Hirota equation. Figure 2(a) shows the actual growth behavior of the unstable perturbation in a three-dimensional evolving plot, highlighting the exponential amplification of the perturbation within a specific wave number range. It is particularly important to note that G represents $|\mathrm{Im}(\Omega)|$, which is always greater than 0. The negative part in the figure is merely a setting for comparing the three-dimensional plot with the density plot in the same figure. Figure 2(b) further presents

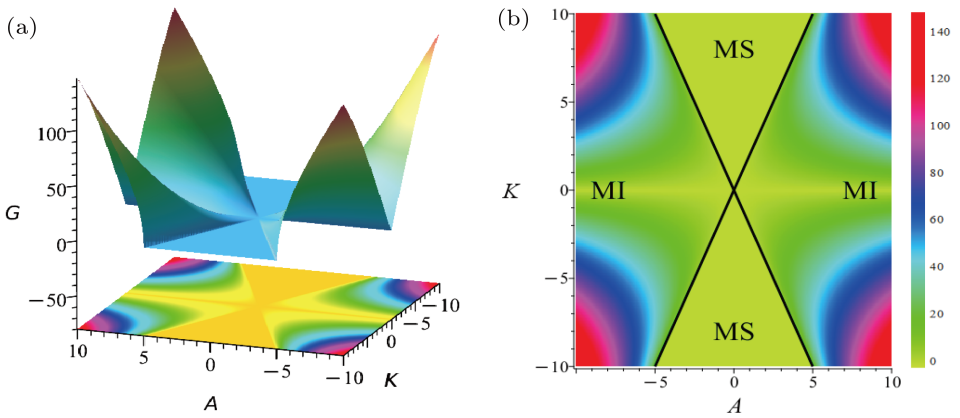


Fig. 2. Three-dimensional and density plots of the MI for the Hirota equation with $\alpha=1$, $\beta=0.1$, and $k=0.5$.

the density plot, where the horizontal axis represents the amplitude A of the perturbation and the vertical axis represents the wavenumber K. Different colors represent different MI gains $G = \mathrm{Im}(\Omega)$, which characterize the rate of exponential growth of the perturbation. The range of wavenumbers with a gain greater than zero, $|K| < |2A|$, is clearly defined.

Specifically, the plane-wave background is unstable to perturbations with wavenumbers K that lie within the interval $|K| < |2A|$. Perturbations with wavenumbers outside this range, $|K| \geq |2A|$, will not grow exponentially and are considered stable. This phenomenon, in which instability is confined to a specific band of low-frequency (long-wavelength) perturbations, is also known as the baseband MI phenomenon.

As the process evolves nonlinearly, this periodic train of pulses can further develop into a series of solitons or, under specific conditions, focus its energy into a single and massive peak, forming a rogue wave. This instability is a strong nonlinear effect. When the background intensity is high, the changes caused by perturbations in the unstable region become more pronounced. This analysis demonstrates that the Hirota equation has the basic mechanism for generating rogue waves and provides a quantitative prediction of the parameter range in which these extreme events may occur.

4. N-soliton solutions of the Hirota equation

The Hirota equation (4) is an important integrable extension of the NLSE, incorporating higher-order dispersion and nonlinear effects. The complete integrability of this equation enables us to utilize methods such as the Darboux transformation to construct the N-soliton solutions of the equation. Starting from a zero seed solution, the N-soliton solutions can be expressed in a compact determinant form[53]

$$q^{[N]} = q - 2i\frac{S_{2n}}{W_{2n}}. \tag{17}$$

Here we set the seed to $q = 0$, S_{2n} and W_{2n} are $2N \times 2N$ matrices. The elements in these matrices are composed of the characteristic functions and spectral parameters related to the Lax pair of the Hirota equation. The specific forms of these matrices are[53]

$$S_{2n} = \begin{vmatrix} f_1 & f_2 & \lambda_1 f_1 & \lambda_1 f_2 & \dots & \lambda_1^{n-1} f_1 & \lambda_1^n f_1 \\ g_1 & g_2 & \lambda_2 g_1 & \lambda_2 g_2 & \dots & \lambda_2^{n-1} g_1 & \lambda_2^n g_1 \\ f_3 & f_4 & \lambda_3 f_3 & \lambda_3 f_4 & \dots & \lambda_3^{n-1} f_3 & \lambda_3^n f_3 \\ g_3 & g_4 & \lambda_4 g_3 & \lambda_4 g_4 & \dots & \lambda_4^{n-1} g_3 & \lambda_4^n g_3 \\ \vdots & \vdots & \vdots & \vdots & \ddots & \vdots & \vdots \\ g_{2n-1} & g_{2n} & \lambda_{2n} g_{2n-1} & \lambda_{2n} g_{2n} & \dots & \lambda_{2n}^{n-1} g_{2n-1} & \lambda_{2n}^n g_{2n-1} \end{vmatrix},$$

$$W_{2n} = \begin{vmatrix} f_1 & f_2 & \lambda_1 f_1 & \lambda_1 f_2 & \dots & \lambda_1^{n-1} f_1 & \lambda_1^{n-1} f_2 \\ g_1 & g_2 & \lambda_2 g_1 & \lambda_2 g_2 & \dots & \lambda_2^{n-1} g_1 & \lambda_2^{n-1} g_2 \\ f_3 & f_4 & \lambda_3 f_3 & \lambda_3 f_4 & \dots & \lambda_3^{n-1} f_3 & \lambda_3^{n-1} f_4 \\ g_3 & g_4 & \lambda_4 g_3 & \lambda_4 g_4 & \dots & \lambda_4^{n-1} g_3 & \lambda_4^{n-1} g_4 \\ \vdots & \vdots & \vdots & \vdots & \ddots & \vdots & \vdots \\ g_{2n-1} & g_{2n} & \lambda_{2n} g_{2n-1} & \lambda_{2n} g_{2n} & \dots & \lambda_{2n}^{n-1} g_{2n-1} & \lambda_{2n}^{n-1} g_{2n} \end{vmatrix}, \tag{18}$$

where

$$\begin{aligned} &\lambda_{2n-1} = u_{2n-1} + \mathrm{i}v_{2n-1}, \ \ \lambda_{2n} = \lambda_{2n-1}^*, \\ &f_{2n-1} = \mathrm{e}^{-\mathrm{i}\lambda_{2n-1}x - (4\beta\mathrm{i}\lambda_{2n-1}^3 + 2\alpha\mathrm{i}\lambda_{2n-1}^2)t}, \\ &f_{2n} = \mathrm{e}^{\mathrm{i}\lambda_{2n-1}x + (4\beta\mathrm{i}\lambda_{2n-1}^3 + 2\alpha\mathrm{i}\lambda_{2n-1}^2)t}, \\ &g_{2n-1} = -f_{2n}^*, \ \ g_{2n} = f_{2n-1}^* \ \ (n = 1, 2, \dots, N). \end{aligned} \tag{19}$$

There have been studies on the exact solutions of the Hirota equation. In this section, we conduct numerical simulations of these basic nonlinear structures. We use the PINN framework to numerically simulate the N-soliton solutions with $N = 1, 2, 3$. We construct a deep neural network to approximate the solution $q(x,t)$, using the exact analytical form mentioned above as the verification benchmark. The training process of the PINN is guided by the physical constraints from the Hirota equation. By comparing the dynamics of the solution predicted by the PINN with the exact solution, we can demonstrate the ability and accuracy of this data-driven deep learning method in capturing the complex propagation and interaction of solitons.

4.1. One-soliton solutions

Setting $N = 1$ in the general framework, the one-soliton solution is obtained. These matrices (Eq. (18)) can be presented in the following form:

$$S_2 = \begin{vmatrix} f_1 & \lambda_1 f_1 \\ g_1 & \lambda_2 g_1 \end{vmatrix}, \ \ W_2 = \begin{vmatrix} f_1 & f_2 \\ g_1 & g_2 \end{vmatrix}. \tag{20}$$

In Eq. (19), with the spectral parameters and their corresponding functions chosen as

$$\begin{aligned} &f_1 = \mathrm{e}^{-\mathrm{i}(u_1 + \mathrm{i}v_1)x - [4\beta\mathrm{i}(u_1 + \mathrm{i}v_1)^3 + 2\alpha\mathrm{i}(u_1 + \mathrm{i}v_1)^2]t}, \\ &f_2 = \mathrm{e}^{\mathrm{i}(u_1 + \mathrm{i}v_1)x + [4\beta\mathrm{i}(u_1 + \mathrm{i}v_1)^3 + 2\alpha\mathrm{i}(u_1 + \mathrm{i}v_1)^2]t}, \\ &\lambda_1 = u_1 + \mathrm{i}v_1, \ \ \lambda_2 = \lambda_1^*, \ \ g_1 = -f_2^*, \ \ g_2 = f_1^*. \end{aligned} \tag{21}$$

The spectral parameter $\lambda_1 = u_1 + \mathrm{i}v_1$ encodes the fundamental properties of the soliton: the propagation velocity and phase evolution are mainly determined by the real part u_1, while the imaginary part v_1 determines both its amplitude and spatial width. The coefficients containing α and β reflect the influence of the higher-order nonlinear and dispersive terms in the Hirota equation (4).

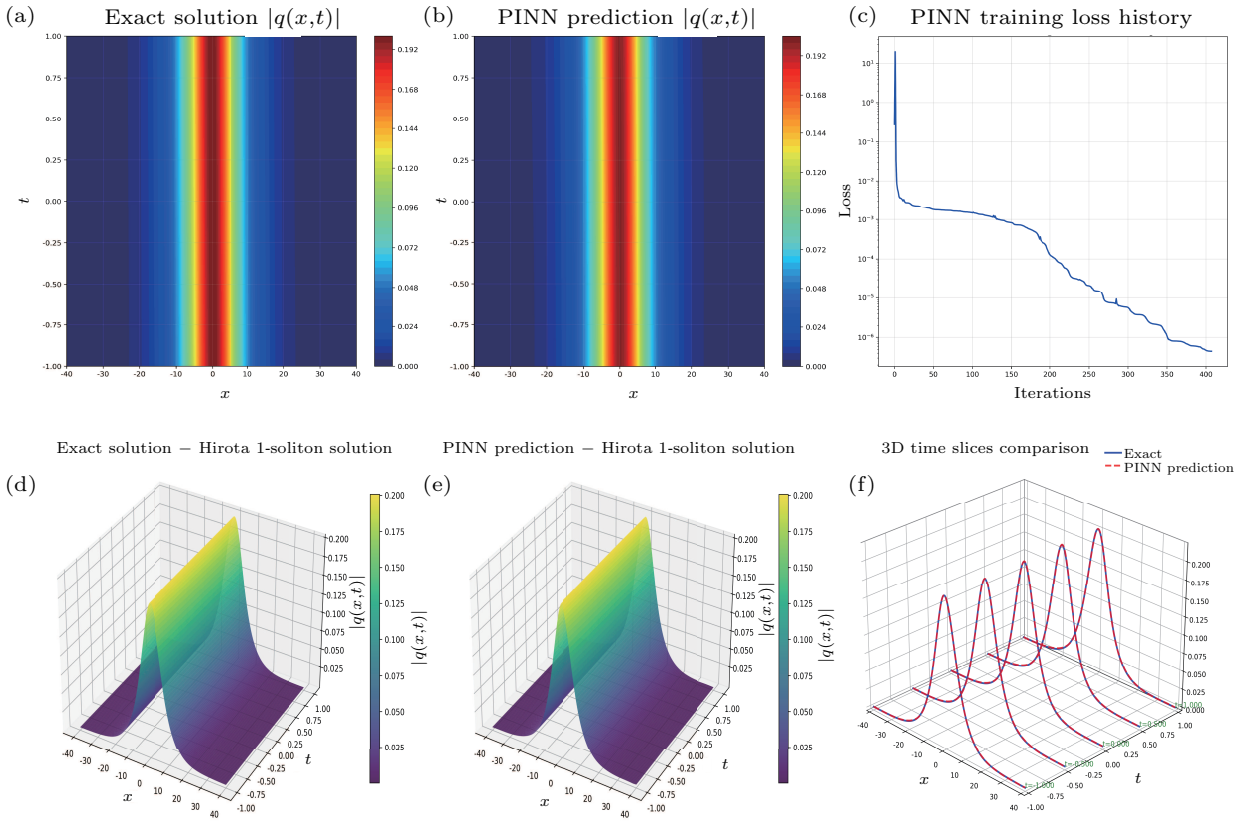


Fig. 3. Comparison of the exact solution in Eq. (22) and the predicted solution for the one-soliton solution at different time points. (a) and (b) Density plots of the exact and predicted solutions, respectively. (c) Training loss curve. (d) and (e) Three-dimensional plots of the exact and predicted solutions, respectively. (f) Three-dimensional comparison plot of five time slices.

Substituting Eqs. (20) and (21) into Eq. (17), we obtain the one-soliton solution

$$\begin{aligned} q^{[1]}(x,t) &= q - 2\mathrm{i}\frac{S_2}{W_2} \\ &= 2v_1\,\mathrm{sech}(-2v_1x-(24\beta v_1u_1^2-8\beta v_1^3+8\alpha v_1u_1)t) \\ &\quad\times \mathrm{e}^{2\mathrm{i}[-u_1x-(4\beta u_1^3+2\alpha u_1^2-12\beta u_1v_1^2-2\alpha v_1^2)t]}. \end{aligned} \tag{22}$$

For numerical simulation, we configured a PINN with a feedforward architecture consisting of 4 hidden layers and 20 neurons per layer, using the tanh activation function. The training data was generated from the exact one-soliton solution Eq. (22) with parameters $\alpha = 1.0$, $\beta = 0.1$, $u_1 = 0.05$, and $v_1 = 0.1$. The spatial domain was divided into 257 equidistant nodes, while the time domain was partitioned into 101 time steps, and an accurate dataset for the soliton solution was subsequently generated using the analytical solution. A total of 200 points were sampled from the initial condition ($t = -1$) and the spatial boundaries ($x = -40$ and $x = 40$). Using the Latin Hypercube Sampling method, 10000 constraint points were randomly selected within the domain of $[-40,40]\times[-1,1]$ to implement the physical constraints. The network was trained by minimizing a composite loss function, comprising the mean squared error on the training data and the mean squared residual of the governing PDEs, and was optimized using the L-BFGS optimizer.

Figure 3 describes the numerical solution of a single bright soliton, which is a stable, localized wave packet with an amplitude of $2v_1$. It does not undergo any deformation during propagation, which is a typical feature of soliton behavior and stems from the precise balance between dispersion and nonlinearity in integrable systems. Figures 3(a) and 3(b) show a density plot comparison between the exact one-soliton solution in Eq. (22) and the PINN-predicted solution. The high-intensity trajectories of the soliton are accurately reproduced by the PINN, with the same slope and color distribution. Figures 3(d) and 3(e) show the spatiotemporal evolution plots. These surfaces are almost indistinguishable, indicating that the PINN has successfully learned the propagation dynamics of the soliton, including its constant speed and stable amplitude.

The historical records of the training process are shown in Fig. 3(c). After 23 seconds and 389 iterations, the relative L_2 error reached 6.744066×10^{-3}. The loss curve observed throughout the training process reveals a rapid decline in the loss function during the initial phase, followed by stabilization and convergence, and finally reached a value of 4.440241×10^{-7}. This smooth convergence curve demonstrates the efficiency of the optimization process and further provides a solid foundation for the accurate results observed in the previous plots. In order to conduct a more detailed assessment, Fig. 3(f) presents the solution profiles at five distinct time slices. The prediction performance of the PINN is shown

in the figure. The predicted solution (red dotted line) almost completely coincides with the exact solution (blue solid line), which further demonstrates that the relative L_2 error remains at a low level. The low error indicates that the predicted solution of the PINN has high accuracy.

4.2. Two-soliton solutions

When $N = 2$, the obtained two-soliton solution describes the interaction between two solitons. In integrable systems, such interactions are typically elastic, meaning that the solitons recover their original shapes and velocities after the collision, leaving the phase shift resulting from the interaction as a residual feature. The precise two-soliton solution is derived based on the general determinant formula (Eq. (17)) for $N = 2$

$$q^{[2]}(x,t) = q - 2\mathrm{i}\frac{S_4}{W_4}. \tag{23}$$

The matrices S_4 and W_4 in the above formula can be expressed as follows:

$$S_4 = \begin{vmatrix} f_1 & f_2 & \lambda_1 f_1 & \lambda_1^2 f_1 \\ g_1 & g_2 & \lambda_2 g_1 & \lambda_2^2 g_1 \\ f_3 & f_4 & \lambda_3 f_3 & \lambda_3^2 f_3 \\ g_3 & g_4 & \lambda_4 g_3 & \lambda_4^2 g_3 \end{vmatrix}, \quad W_4 = \begin{vmatrix} f_1 & f_2 & \lambda_1 f_1 & \lambda_1 f_2 \\ g_1 & g_2 & \lambda_2 g_1 & \lambda_2 g_2 \\ f_3 & f_4 & \lambda_3 f_3 & \lambda_3 f_4 \\ g_3 & g_4 & \lambda_4 g_3 & \lambda_4 g_4 \end{vmatrix}, \tag{24}$$

where the matrices S_4 and W_4 are constructed using two distinct spectral parameters λ_1 and λ_3 and their corresponding functions

$$\begin{aligned} f_1 &= \mathrm{e}^{-\mathrm{i}(u_1+\mathrm{i}v_1)x-[4\beta\mathrm{i}(u_1+\mathrm{i}v_1)^3+2\alpha\mathrm{i}(u_1+\mathrm{i}v_1)^2]t}, \\ f_2 &= \mathrm{e}^{\mathrm{i}(u_1+\mathrm{i}v_1)x+[4\beta\mathrm{i}(u_1+\mathrm{i}v_1)^3+2\alpha\mathrm{i}(u_1+\mathrm{i}v_1)^2]t}, \\ f_3 &= \mathrm{e}^{-\mathrm{i}(u_3+\mathrm{i}v_3)x-[4\beta\mathrm{i}(u_3+\mathrm{i}v_3)^3+2\alpha\mathrm{i}(u_3+\mathrm{i}v_3)^2]t}, \\ f_4 &= \mathrm{e}^{\mathrm{i}(u_3+\mathrm{i}v_3)x+[4\beta\mathrm{i}(u_3+\mathrm{i}v_3)^3+2\alpha\mathrm{i}(u_3+\mathrm{i}v_3)^2]t}, \\ \lambda_1 &= u_1+\mathrm{i}v_1, \ \lambda_3 = u_3+\mathrm{i}v_3, \ \lambda_2 = \lambda_1^*, \ \lambda_4 = \lambda_3^*, \\ g_1 &= -f_2^*, \ g_2 = f_1^*, \ g_3 = -f_4^*, \ g_4 = f_3^*. \end{aligned} \tag{25}$$

For the PINN simulation, since the equation obtained after simplifying the matrix determinant is quite complex, we directly input the above matrix and parameters into the PINN architecture for simulation. The selected parameters are $\alpha = 1.0$, $\beta = 0.1$, $u_1 = 0.8$, $v_1 = 0.5$, $u_3 = 0.0$, and $v_3 = 0.5$. A corresponding finite-difference grid was constructed, which divided the spatial domain into 257 equally spaced nodes and the time domain into 101 time steps, ultimately yielding an accurate dataset for the soliton solutions. A slightly larger neural network was used, with 4 hidden layers and 50 neurons in each layer. The training domain was set as $x \in [-15, 15]$ and $t \in [-1, 1]$. The training dataset included 200 points on the initial condition ($t = -1$) and spatial boundaries ($x = -15$ and $x = 15$), all from the exact solution. A total of 10000 collocation points were used to enforce the Hirota equation. The training process followed the L-BFGS optimization strategy. The PINN demonstrates its expressivity by handling two-soliton

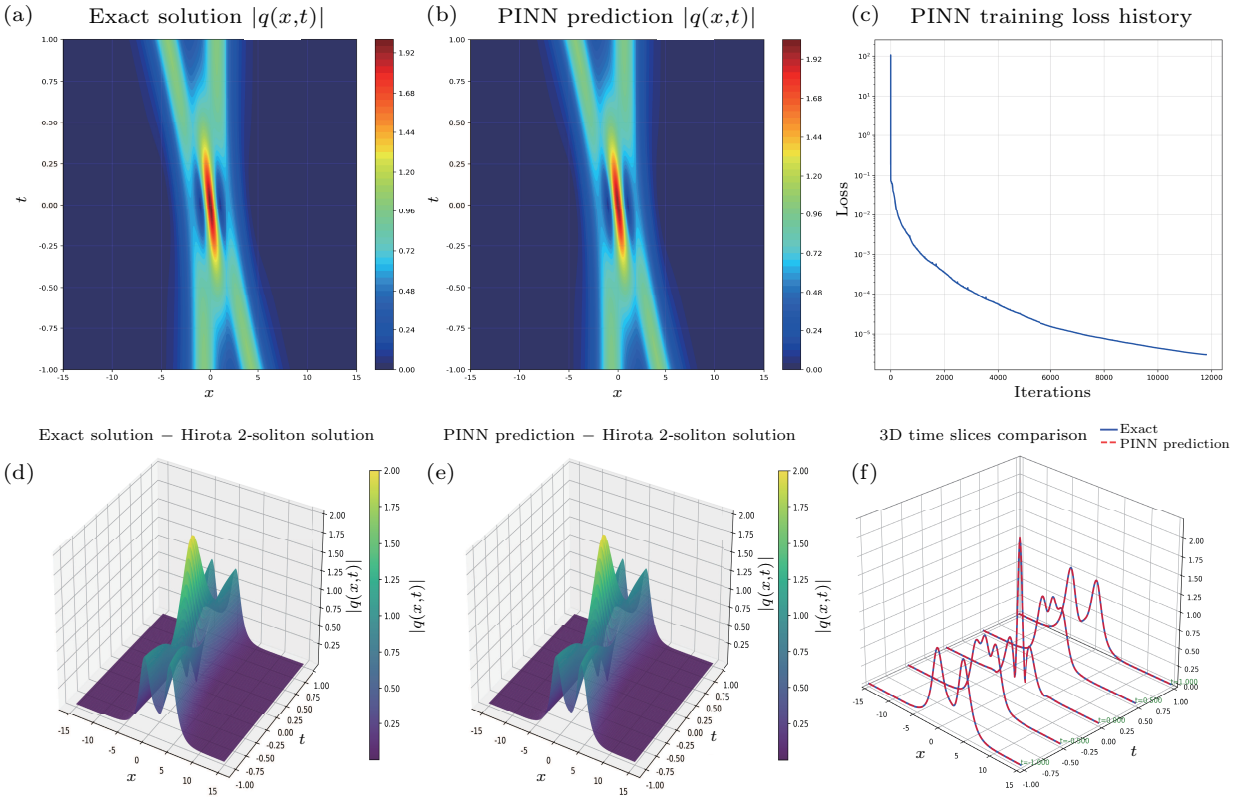


Fig. 4. Comparison of the exact solution in Eq. (23) and the predicted solution for the two-soliton solution at different time points. (a) and (b) Density plots of the exact and predicted solutions, respectively. (c) Training loss curve. (d) and (e) Three-dimensional plots of the exact and predicted solutions, respectively. (f) Three-dimensional comparison plot of five time slices.

solutions with interactions through sparse data.

The results of the two-soliton simulation are presented in Fig. 4. The density plots in Figs. 4(a) and 4(b) show the top views of the two solitons and their intersecting trajectories with high fidelity. The three-dimensional surface plots in Figs. 4(d) and 4(e) clearly depict the collision process. The PINN-predicted surface on the right is visually identical to the exact solution on the left. These peaks undergo a definite interaction, during which they collide nonlinearly, temporarily changing their shapes and forming wave peaks. However, they subsequently separate and maintain their respective characteristics. The PINN achieves extremely high accuracy and is capable of accurately capturing the trajectories of the two solitons before, during, and after their interaction, including their characteristic phase changes.

The training loss curve in Fig. 4(c) shows a consistent decrease. After 337 seconds and 10919 iterations, the loss converged to a final value of 3.055232×10^{-6}, and the relative L_2 error remained low, reaching 2.802835×10^{-3}. The time-slice comparisons in Fig. 4(f) provide a quantitative assessment of the model's accuracy throughout the interaction. The evolution shown in this figure reveals the entire dynamic formation process of the solitons from the background, clearly capturing the appearance of two prominent wave peaks, their brief fusion during the collision, and their subsequent separation. At time points $t = -1.0$ (before the collision), $t = 0.0$ (peak interaction), and $t = 1.0$ (after the collision), the waveforms predicted by the PINN are highly consistent with the exact waveforms. The successful simulation of this interaction demonstrates the ability of the PINN to study various complex nonlinear dynamical systems.

4.3. Three-soliton solutions

When $N = 3$, Eq. (17) represents the three-soliton solution, describing the synchronous interaction of three solitons. The interaction of three solitons is much more complex than the collision of two solitons, involving a series of pairwise collisions, which leads to complex phase changes for each soliton. Its analytical form is given by the general determinant formula for $N = 3$

$$q^{[3]}(x,t) = q - 2\mathrm{i}\frac{S_6}{W_6}. \tag{26}$$

The matrices S_6 and W_6 can be presented in the following form:

$$S_6 = \begin{vmatrix} f_1 & f_2 & \lambda_1 f_1 & \lambda_1 f_2 & \lambda_1^2 f_1 & \lambda_1^3 f_1 \\ g_1 & g_2 & \lambda_2 g_1 & \lambda_2 g_2 & \lambda_2^2 g_1 & \lambda_2^3 g_1 \\ f_3 & f_4 & \lambda_3 f_3 & \lambda_3 f_4 & \lambda_3^2 f_3 & \lambda_3^3 f_3 \\ g_3 & g_4 & \lambda_4 g_3 & \lambda_4 g_4 & \lambda_4^2 g_3 & \lambda_4^3 g_3 \\ f_5 & f_6 & \lambda_5 f_5 & \lambda_5 f_6 & \lambda_5^2 f_5 & \lambda_5^3 f_5 \\ g_5 & g_6 & \lambda_6 g_5 & \lambda_6 g_6 & \lambda_6^2 g_5 & \lambda_6^3 g_5 \end{vmatrix},$$

$$W_6 = \begin{vmatrix} f_1 & f_2 & \lambda_1 f_1 & \lambda_1 f_2 & \lambda_1^2 f_1 & \lambda_1^2 f_2 \\ g_1 & g_2 & \lambda_2 g_1 & \lambda_2 g_2 & \lambda_2^2 g_1 & \lambda_2^2 g_2 \\ f_3 & f_4 & \lambda_3 f_3 & \lambda_3 f_4 & \lambda_3^2 f_3 & \lambda_3^2 f_4 \\ g_3 & g_4 & \lambda_4 g_3 & \lambda_4 g_4 & \lambda_4^2 g_3 & \lambda_4^2 g_4 \\ f_5 & f_6 & \lambda_5 f_5 & \lambda_5 f_6 & \lambda_5^2 f_5 & \lambda_5^2 f_6 \\ g_5 & g_6 & \lambda_6 g_5 & \lambda_6 g_6 & \lambda_6^2 g_5 & \lambda_6^2 g_6 \end{vmatrix}, \tag{27}$$

where the matrices S_6 and W_6 are constructed using three distinct spectral parameters λ_1, λ_3, and λ_5 and their corresponding functions

$$\begin{aligned}
f_1 &= \mathrm{e}^{-\mathrm{i}(u_1+\mathrm{i}v_1)x-(4\beta\mathrm{i}(u_1+\mathrm{i}v_1)^3+2\alpha\mathrm{i}(u_1+\mathrm{i}v_1)^2)t}, \\
f_2 &= \mathrm{e}^{\mathrm{i}(u_1+\mathrm{i}v_1)x+(4\beta\mathrm{i}(u_1+\mathrm{i}v_1)^3+2\alpha\mathrm{i}(u_1+\mathrm{i}v_1)^2)t}, \\
f_3 &= \mathrm{e}^{-\mathrm{i}(u_3+\mathrm{i}v_3)x-(4\beta\mathrm{i}(u_3+\mathrm{i}v_3)^3+2\alpha\mathrm{i}(u_3+\mathrm{i}v_3)^2)t}, \\
f_4 &= \mathrm{e}^{\mathrm{i}(u_3+\mathrm{i}v_3)x+(4\beta\mathrm{i}(u_3+\mathrm{i}v_3)^3+2\alpha\mathrm{i}(u_3+\mathrm{i}v_3)^2)t}, \\
f_5 &= \mathrm{e}^{-\mathrm{i}(u_5+\mathrm{i}v_5)x-(4\beta\mathrm{i}(u_5+\mathrm{i}v_5)^3+2\alpha\mathrm{i}(u_5+\mathrm{i}v_5)^2)t}, \\
f_6 &= \mathrm{e}^{\mathrm{i}(u_5+\mathrm{i}v_5)x+(4\beta\mathrm{i}(u_5+\mathrm{i}v_5)^3+2\alpha\mathrm{i}(u_5+\mathrm{i}v_5)^2)t}, \\
\lambda_1 &= u_1+\mathrm{i}v_1, \quad \lambda_3 = u_3+\mathrm{i}v_3, \quad \lambda_5 = u_5+\mathrm{i}v_5, \\
\lambda_2 &= \lambda_1^*, \quad \lambda_4 = \lambda_3^*, \quad \lambda_6 = \lambda_5^*, \\
g_1 &= -f_2^*, \quad g_2 = f_1^*, \quad g_3 = -f_4^*, \\
g_4 &= f_3^*, \quad g_5 = -f_6^*, \quad g_6 = f_5^*.
\end{aligned} \tag{28}$$

We employed a deeper and wider PINN architecture with 5 hidden layers and 100 neurons per layer. The chosen parameters for the exact solution were $\alpha = 1.0$, $\beta = 0.1$, $u_1 = 0.8$, $v_1 = 0.5$, $u_3 = 0.0$, $v_3 = 0.5$, $u_5 = -0.8$, and $v_5 = 0.5$. A corresponding finite-difference grid was established, which divided the spatial domain into 257 equally spaced nodes and the time domain into 101 time steps, ultimately yielding an accurate dataset of soliton solutions. The computational domain was $x \in [-16, 16]$ and $t \in [-2, 2]$. The training set included 300 points from the initial condition ($t = -2$) and the spatial boundaries ($x = -16$ and $x = 16$), while the physics loss was enforced on a large set of 15000 collocation points. The training procedure followed the same L-BFGS optimization strategy.

The simulation results are shown in Fig. 5. The density plots in Figs. 5(a) and 5(b) clearly display these complex trajectories from top to bottom, and the results of the PINN are highly consistent with the exact solution. The three-dimensional plots in Figs. 5(c) and 5(d) show the complex interactions of three solitons. The PINN successfully predicted the entire interaction process, and the three-soliton solutions present a main central peak and smaller-amplitude peaks on both sides, forming a distinct three-peak structure. Unlike simple pairwise collisions, this structure demonstrates more complex and coherent interactions, where all three solitons are simultaneously involved, resulting in a stable composite waveform, including the faster soliton overtaking the slower soliton and the resulting phase changes.

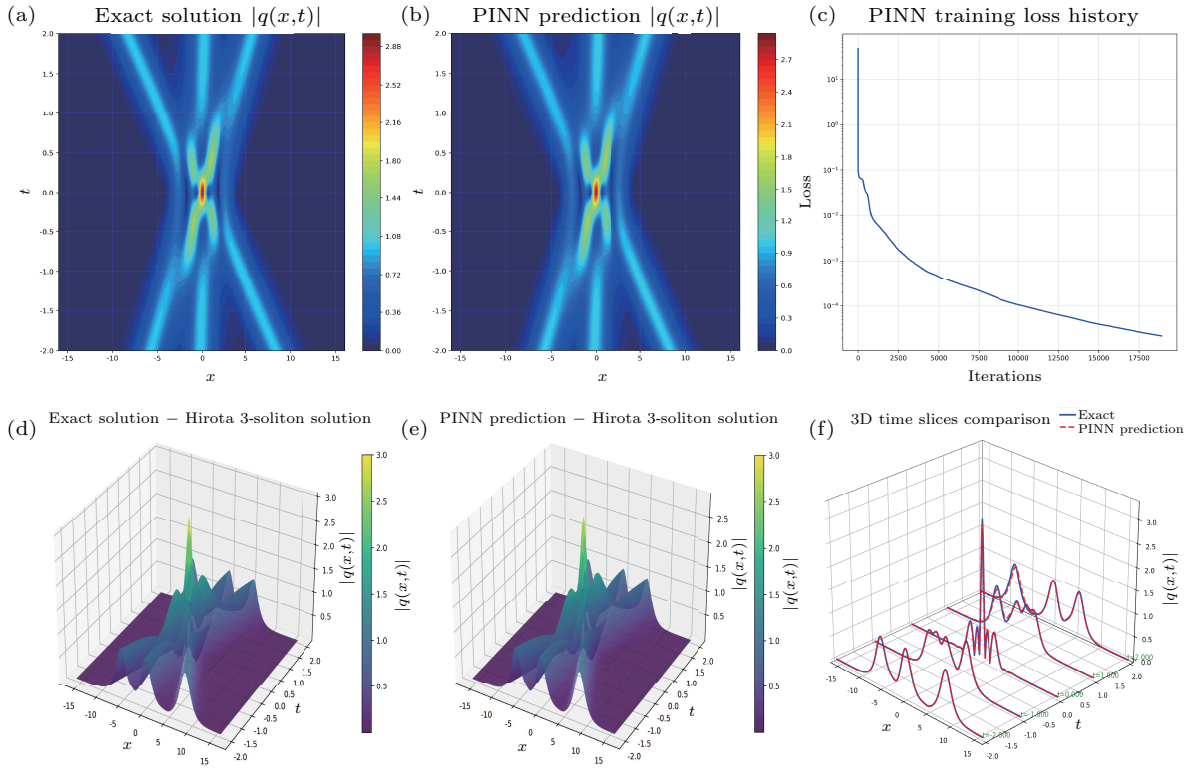


Fig. 5. Comparison of the exact solution in Eq. (26) and the predicted solution for the three-soliton solution at different time points. (a) and (b) Density plots of the exact and predicted solutions, respectively. (c) Training loss curve. (d) and (e) Three-dimensional plots of the exact and predicted solutions, respectively. (f) Three-dimensional comparison plot of five time slices.

The loss curve in Fig. 5(c) indicates that, despite the various challenges associated with this problem, the training process eventually converged to a relatively low loss value of 2.247597×10^{-5} after 1286 seconds and 17500 iterations, with a relative L_2 error of 5.050334×10^{-2}, which validates the reliability of the obtained solution. The time-slice comparison in Fig. 5(f) demonstrates the accuracy of the model at different stages of the complex interactions. Even during the collision stage with highly structured waveforms ($t = 0.0$), the PINN maintained high accuracy. Given the high complexity of the three-soliton solutions and the low error of the numerical solution over a wide range of space and time, the fitting performance of this numerical method is excellent. The comparison with the exact solution effectively shows that the PINN model can not only replicate a single wave peak but also accurately reproduce the subtle interference dynamics and phase changes of three wave systems, highlighting the reliability and effectiveness of the PINN in studying various dynamical structures of nonlinear partial differential equations and demonstrating its great potential for studying the interactions of multiple wave systems.

5. The N-order rogue wave solutions of the Hirota equation

The study of nonlinear wave phenomena holds a central position in numerous fields of physics, and rogue waves are an important component among them. Next, we investigate the Hirota equation with high-order dispersion and nonlinear effects Eq. (4).

The complete integrability of this equation enables the derivation of exact analytical solutions, including soliton solutions, breathing solutions, and rogue wave solutions. Rogue waves are highly special and localized phenomena, and the study of these phenomena is crucial for understanding extreme events in various physical systems. Although some powerful computational methods play a crucial role in deriving analytical solutions of the Hirota equation (4) and understanding the hierarchical structure of solitons, exploring the dynamic behavior under more general conditions or for non-integrable variants requires powerful numerical methods. PINN achieves accurate computational results by embedding the Hirota equation (4) into the loss function of the neural network, learning solutions that satisfy the physical constraints from sparse data, and continuously minimizing the error. The PINN method has been successfully applied to a variety of complex nonlinear systems and has demonstrated excellent numerical performance in solving rogue wave solutions of equations.

This part uses the PINN framework to numerically simulate the rogue wave solutions of the Hirota equation and verifies the solutions by comparing them with the exact analytical solutions to confirm their accuracy. We approximate the numerical solution $q(x,t)$ by constructing a deep neural network that incorporates physical constraints, ensuring that the solution conforms to the physical properties of the Hirota equa-

tion. Specifically, we investigate the capability of the PINN in solving the complex spatiotemporal structures of the first- and second-order rogue wave solutions and demonstrate the potential of this data-driven computational method for studying extreme nonlinear wave phenomena.

5.1. First-order rogue wave solutions

The first-order rogue wave solutions of the Hirota equation can be obtained as a limit of the breather solution. A simplified yet representative form of the first-order rogue wave is obtained[53]

$$q_{\text{rogue}}^{[1]} = \mathrm{e}^{\mathrm{i}bt}\sqrt{\frac{b}{2\alpha}}\frac{-2b\alpha^2x^2+12b^2\alpha\beta xt-18b^3\beta^2t^2-4b^2\alpha^3t^2+8\mathrm{i}b\alpha^3t+3\alpha^3}{4b^2\alpha^3t^2+2b\alpha^2x^2-12b^2\alpha\beta xt+18b^3\beta^2t^2+\alpha^3}. \tag{29}$$

This solution describes a single wave packet that is localized in both space and time. Its structure is governed by the parameters α, β, and b, which allows for a degree of control over its characteristics, a feature that is valuable for potential experimental verification. When $\beta = 0$, this solution correctly reduces to the well-known Peregrine soliton of the standard NLSE. The parameter b is the coefficient of the frequency term in the phase of the background plane wave and is intrinsically linked to the background amplitude and wavenumber through the dispersion relation of the Hirota equation. In the first-order rogue wave solution Eq. (29), under the specified conditions, b primarily determines the background intensity and the spatiotemporal scaling of the rogue wave envelope, influencing its peak amplitude and localization width. The parameters α and β are the coefficients of the standard- and higher-order terms in the Hirota equation, governing nonlinearity, dispersion, and higher-order effects, respectively.

The spatiotemporal domain is defined as $x \in [-5.0, 5.0]$ and $t \in [-1.0, 1.0]$. The parameters for the exact solution are set to $\alpha = 1.0$, $\beta = 0.1$, and $b = 1.0$. We divide the spatial domain $[-5, 5]$ into 257 equally spaced nodes and the time domain $[-1, 1]$ into 101 time steps, thereby generating an accurate dataset of rogue wave solutions. The training dataset is constructed using a two-stage sampling strategy. First, $N_{\text{q}} = 200$ data points are randomly selected from the initial and boundary conditions, which are derived from the exact analytical solution at $t = -1.0$ and $x = \pm 5.0$. These points anchor the model to the known solution behavior. Second, $N_{\text{f}} = 10000$ collocation points are sampled from the interior of the domain using Latin Hypercube Sampling to enforce the Hirota equation residual. For the PINN architecture, there are 4 hidden layers, each containing 50 neurons. The network is trained using the L-BFGS optimizer to minimize the combined data and physics loss.

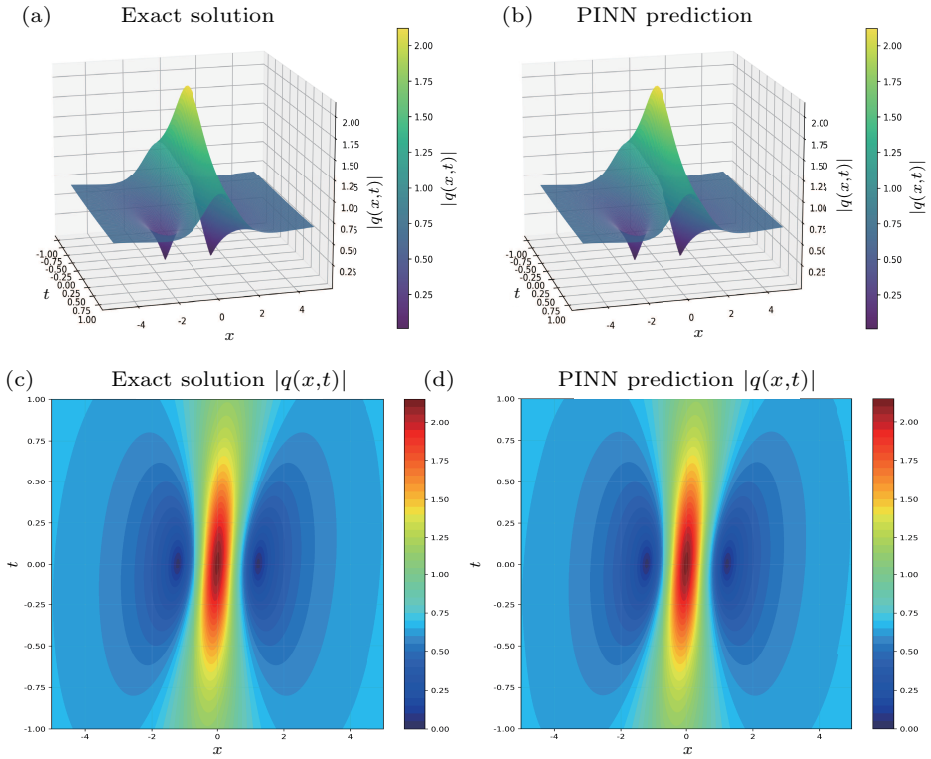


Fig. 6. Comparison of the exact analytical solution in Eq. (29) and the PINN-predicted solution for the first-order rogue wave solution. (a) and (b) Three-dimensional plots of the exact and predicted solutions, respectively. (c) and (d) Density plots of the exact and predicted solutions, respectively.

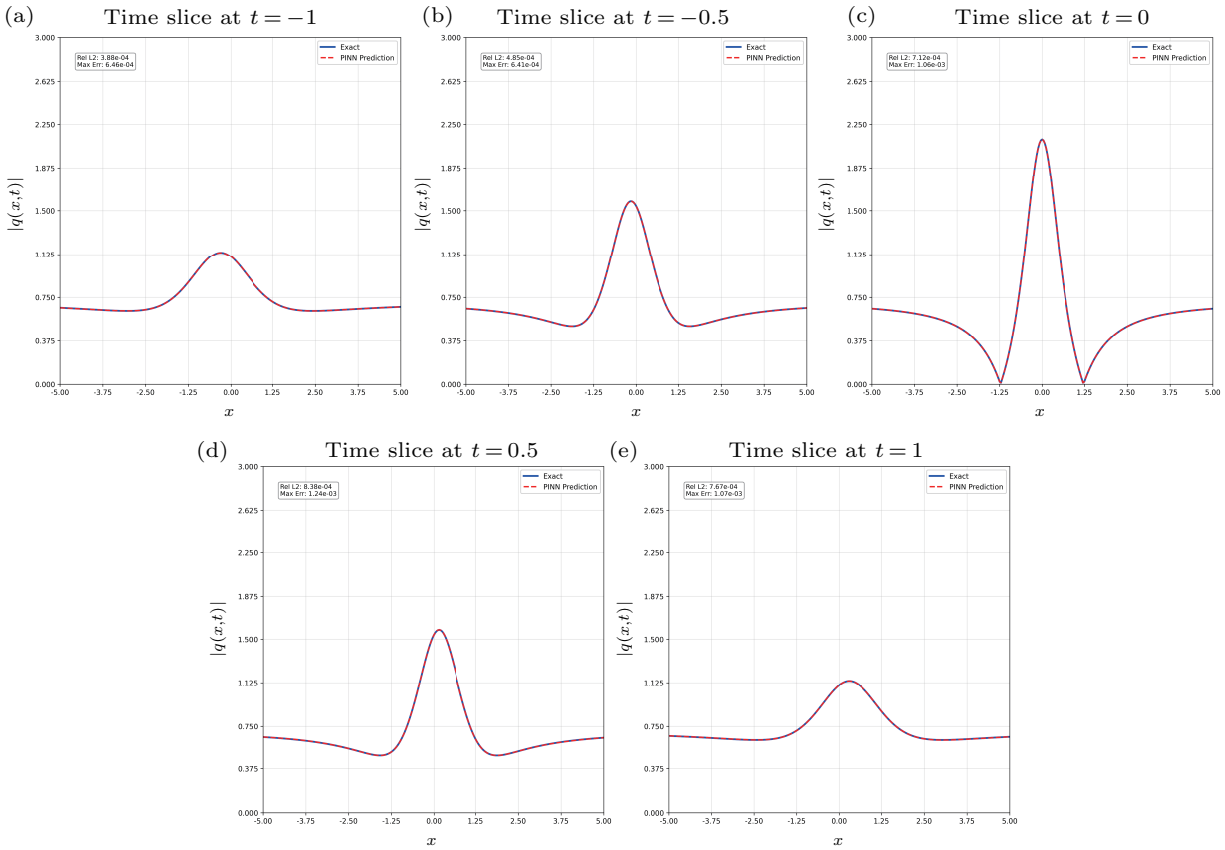


Fig. 7. Cross-sections of the exact analytical solution in Eq. (29) and the PINN-predicted solution for the first-order rogue wave at $t=-1.0$, $t=-0.5$, $t=0.0$, $t=0.5$, and $t=1.0$, shown in panels (a), (b), (c), (d), and (e), respectively.

The results of the PINN simulation are presented in Fig. 6. Figures 6(a) and 6(b) show the three-dimensional surface plots of the exact solution (left) and the PINN-predicted solution (right). The plots demonstrate that the PINN has successfully captured the defining characteristic of the first-order rogue wave: the solution exhibits a characteristic, highly localized peak that emerges abruptly from a nearly uniform background before rapidly decaying. This single, transient structure lacks the persistent multi-peak profile of a soliton, instead manifesting as a sudden and intense concentration of energy within a compact region of space-time. It emerges from a constant background and recedes back into it. The amplitude, shape, and localization of the predicted waveform over the entire plane are in excellent visual agreement with those of the exact solution. This is further confirmed by the density plots in Figs. 6(c) and 6(d), where the intensity distribution and the orientation of the high-amplitude region in the PINN prediction (right) are nearly indistinguishable from those of the exact solution (left).

To conduct a more accurate assessment, Fig. 7 presents a cross-sectional comparison at five different time points: $t=-1.0$, $t=-0.5$, $t=0.0$, $t=0.5$, and $t=1.0$. In each time slice, the exact solution (blue solid line) is compared with the PINN prediction (red dashed line). Throughout the different stages of the rogue wave evolution, this consistency is highly significant. At $t=0.0$, the PINN accurately reproduces the maximum peak amplitude, which is approximately three times the background value. At earlier ($t=-0.5$) and later ($t=0.5$) time points, the model correctly captures the broadening and weakening of the wave packet. After 228 seconds and 7418 iterations, the relative L_2 error reached 6.951301×10^{-4}. During the training process, the final loss value converged from 10^{-1} to 2.951604×10^{-6}, which verifies the reliability of the obtained solution. The small error confirms that the PINN method has high accuracy in simulating the dynamic structure of first-order rogue waves. This successful application highlights the ability of the PINN to learn complex and transient solutions from limited data, providing a powerful tool for the study of such nonlinear systems.

5.2. Second-order rogue wave solutions

Higher-order rogue waves represent more complex and extreme events, often described as the nonlinear superposition of fundamental rogue waves. The second-order rogue wave solution of the Hirota equation has a more complex structure, typically featuring a central peak with an amplitude higher than that of the first-order rogue wave solution, together with smaller secondary peaks around it. The analytical expression for this solution is considerably more complex and can be derived using a modified Darboux transformation scheme.[42]

The solution takes the form

$$q^{[2]}_{\text{rogue}}(x,t) = \mathrm{e}^{\mathrm{i}x}\left(1+\frac{G_2+\mathrm{i}xH_2}{D_2}\right), \tag{30}$$

where G_2, H_2, and D_2 are high-order polynomials in the spatiotemporal coordinates x and t, whose coefficients depend on the higher-order parameter β. When the coefficients of the group-velocity dispersion and the Kerr nonlinearity are set to $\alpha = 1/2$, the explicit forms of these polynomials are given by

$$\begin{aligned} G_2 \;=\; & 12\Big\{-16t^4+384\beta xt^3-24[4(36\beta^2+1)x^2+1]t^2 \\ & +96\beta x[12(12\beta^2+1)x^2+7]t \\ & -16(1296\beta^4+216\beta^2+5)x^4 \\ & -72(44\beta^2+1)x^2+3\Big\}, \end{aligned} \tag{31}$$

$$\begin{aligned} H_2 \;=\; & 24\Big\{-16t^4+384\beta xt^3-8[(432\beta^2+4)x^2-3]t^2 \\ & +96\beta xt[4(36\beta^2+1)x^2+1]-16(36\beta^2+1)^2x^4 \\ & -8(180\beta^2+1)x^2+15\Big\}, \end{aligned} \tag{32}$$

$$\begin{aligned} D_2 \;=\; & 64t^6-2304\beta xt^5-432(624\beta^4-40\beta^2-1)x^4 \\ & +36(556\beta^2+11)x^2+9+64(36\beta^2+1)^3x^6 \\ & -384\beta t^3[12(60\beta^2+1)x^2-1]x \\ & +48t^4[(720\beta^2+4)x^2+1] \\ & +12\Big[16(6480\beta^4+216\beta^2+1)x^4 \\ & -24(60\beta^2+1)x^2+9\Big]t^2 \\ & -144\beta x\Big[16(36\beta^2+1)^2x^4 \\ & +(8-864\beta^2)x^2+17\Big]t. \end{aligned} \tag{33}$$

The complexity of this solution poses significant challenges to numerical methods. To enable the PINN framework to accurately capture this complex structure, we consider the spatiotemporal domain $x \in [-3.0, 3.0]$ and $t \in [-1.0, 1.0]$. The parameter is set to $\beta = 0.1$. We establish the corresponding finite-difference grid, dividing the spatial domain $[-3, 3]$ into 257 equally spaced nodes and the time domain $[-1, 1]$ into 101 time steps, thereby generating an accurate dataset of rogue wave solutions. Due to the increased complexity, we improve the processing capacity and sampling density of the model. The training data consist of $N_{\text{q}} = 300$ data points, which are obtained from the exact analytical solution based on the behavior at $t = -1.0$ and $x = \pm 3.0$. At the same time, the number of interior collocation points is increased to $N_{\text{f}} = 15000$. For the PINN architecture, there are 5 hidden layers, each containing 100 neurons. The network is trained using the L-BFGS optimizer to minimize the combined data and physics loss.

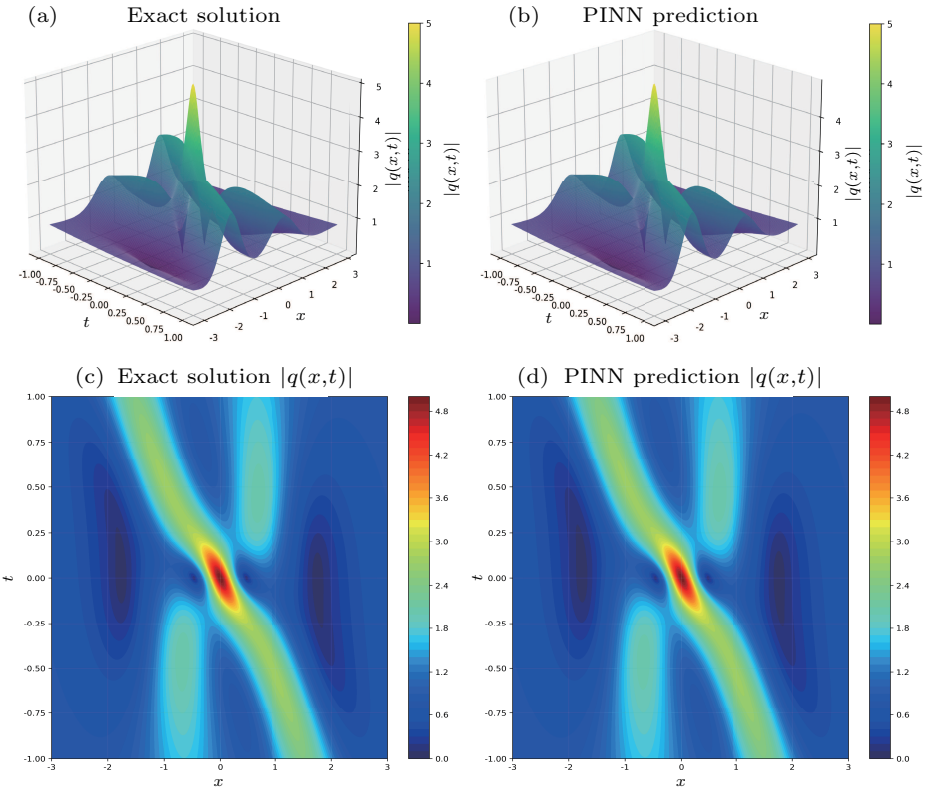


Fig. 8. Comparison of the exact analytical solution in Eq. (30) and the PINN-predicted solution for the second-order rogue wave solution. (a) and (b) Three-dimensional plots of the exact and predicted solutions, respectively. (c) and (d) Density plots of the exact and predicted solutions, respectively.

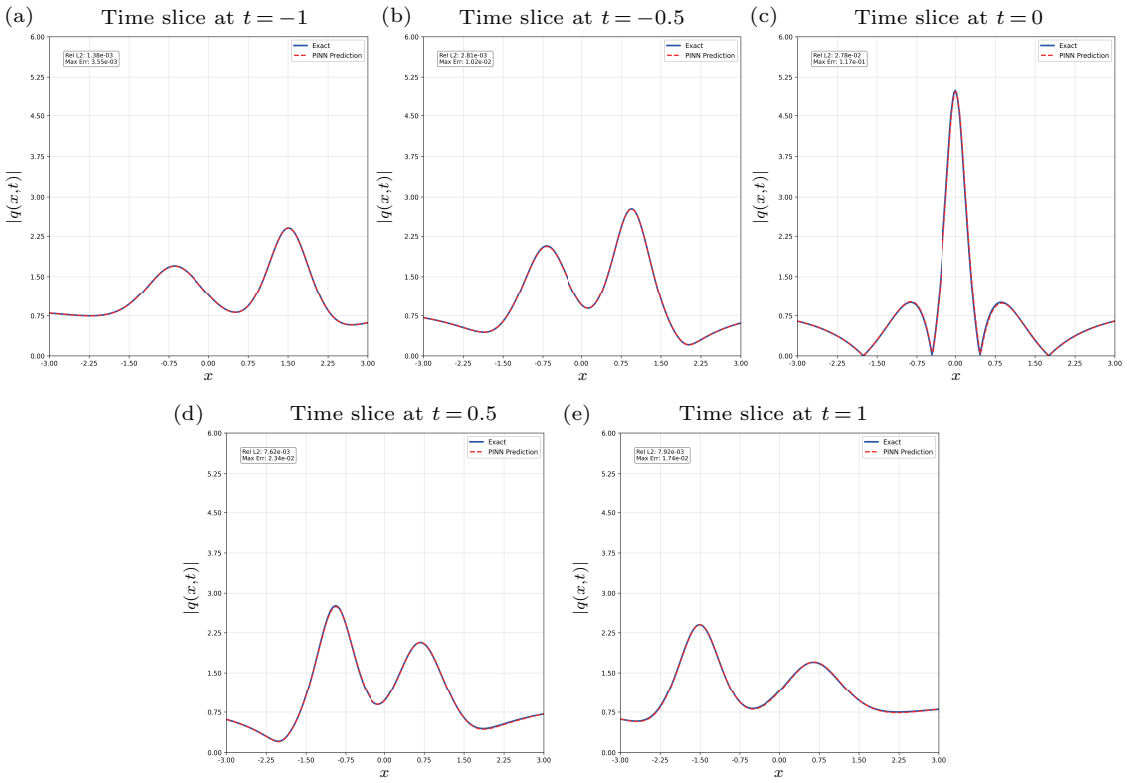


Fig. 9. Cross-sections of the exact analytical solution in Eq. (30) and the PINN-predicted solution for the second-order rogue wave at $t=-1.0$, $t=-0.5$, $t=0.0$, $t=0.5$, and $t=1.0$, shown in panels (a), (b), (c), (d), and (e), respectively.

Figure 8 presents the simulation results of the second-order rogue wave solution. The three-dimensional surface plot in Fig. 8(a) reveals the characteristic structure of the second-order rogue wave, with a prominent main peak at its core, surrounded by several distinct side peaks. These side peaks continuously change over time, thus forming a complex structure. Their dynamic behavior occurs within a fixed spatiotemporal region, where local energy gradually concentrates in the central region and then disperses. The PINN prediction in Fig. 8(b) accurately reproduces this complex structure, including the relative amplitudes and positions of the main and subsidiary peaks. The maximum amplitude of the central peak is approximately five times the background level, and the model also accurately captures this feature. Figures 8(c) and 8(d) show density plots, further demonstrating the success of the model and indicating that, even for complex and high-intensity patterns, the exact solution and the PINN prediction are in close agreement.

The cross-sectional plots in Fig. 9 provide a detailed quantitative comparison at $t=-1.0$, $t=-0.5$, $t=0.0$, $t=0.5$, and $t=1.0$. At $t=0.0$, the PINN solution aligns closely with the exact solution at the central peak. At $t=-1.0$ and $t=1.0$, the model accurately captures the evolution of the wave into a three-peak structure. The blue solid line and the red dashed line are almost indistinguishable at all positions, indicating that the overall deviation is very small. After 1164 seconds and 11400 iterations, the relative L_2 error is 1.776767×10^{-2}, and the training process eventually converges to a loss value of 7.570173×10^{-5}. Especially for such a complex equation over a large spatial and temporal domain, this training performance demonstrates that the PINN has excellent performance in analyzing the multiscale features and complex interactions inherent in high-order wave dynamics. The successful fitting and solution of complex integrable systems such as the Hirota equation and their related discrete models fully demonstrate the flexibility and powerful capabilities of the PINN method in advancing nonlinear scientific research.

6. Conclusion

In this study, we first conducted a theoretical analysis of the modulational instability (MI) of the Hirota equation to determine the parameter conditions favorable for the formation of rogue wave solutions. The model successfully simulated the propagation and elastic collisions of one-, two-, and three-soliton solutions, as well as the highly localized and transient dynamics of first- and second-order rogue wave solutions, accurately capturing their characteristic phase changes and preservation of their shapes after interactions. In particular, the dynamics of the two- and three-soliton solutions and the second-order rogue wave solutions are often difficult to capture using traditional numerical methods. Table 1 summarizes the simulation performance of the PINN for different solutions of the Hirota equation. All cases achieved relatively low relative L_2 errors (ranging from 10^{-4} to 10^{-2} in

order of magnitude) and converged to low loss values (ranging from 10^{-7} to 10^{-5} in order of magnitude). These results indicate that the PINN serves as a powerful, efficient, and mesh-free numerical tool for exploring various nonlinear dynamical characteristics of the Hirota equation and similar integrable systems.

Table 1. Summary of PINN simulation performance for various solutions of the Hirota equation.

Solution type	Spatiotemporal domain	Relative L_2 error	Final convergence loss
One-soliton	$[-40,40]\times[-1,1]$	6.74×10^{-3}	4.44×10^{-7}
Two-soliton	$[-15,15]\times[-1,1]$	2.80×10^{-3}	3.06×10^{-6}
Three-soliton	$[-16,16]\times[-2,2]$	5.05×10^{-2}	2.25×10^{-5}
First-order rogue wave	$[-5,5]\times[-1,1]$	6.95×10^{-4}	2.95×10^{-6}
Second-order rogue wave	$[-3,3]\times[-1,1]$	1.78×10^{-2}	7.57×10^{-5}

The emergence of PINNs provides a transformative approach to solving complex partial differential equations by combining the powerful function approximation capability of deep learning with strict physical laws. Previous studies have applied PINNs to investigate basic solutions of the Hirota equation,[54] but the comprehensive solution and systematic exploration of more complex solution families, such as multi-soliton solutions and high-order rogue wave solutions, remain challenging. The main innovation of this study lies in the first use of a unified PINN framework for the systematic application to the complete solution and analysis of the Hirota equation, including N-soliton wave solutions ($N = 1, 2, 3$) and N-order rogue wave solutions ($N = 1, 2$). The framework achieves excellent numerical performance, demonstrating its ability to handle the Hirota equation and complex nonlinear wave interactions in partial differential equations.

This study also reveals some limitations of this method. During long-term time simulations, errors may accumulate, which may reduce the accuracy of predictions over larger spatial and temporal scales. Additionally, due to the spectral bias of PINNs, the model's ability to solve problems with complex structures or steep gradients, such as the peak amplitudes of high-order rogue wave solutions or the collision stages of multiple solitons, may be limited. To address these issues, future work will extend the application of this framework to broader spatial and temporal scales. Proposed improvements include adaptive sampling based on residuals and dynamic weighting strategies to better capture regions with highly dynamic changes. Domain decomposition techniques will also be adopted, combined with a network architecture that follows physical conservation laws, to improve numerical stability and generalization ability. Moreover, mixed optimization strategies, such as Adam and L-BFGS, can be used to enhance the optimization efficiency of the solution process. This study further confirms that PINNs provide a flexible and powerful paradigm for computational research in nonlinear science, offering an effective framework for a deeper understanding of complex wave dynamics and achieving more reliable predictions.

Acknowledgments

Project supported by the National Natural Science Foundation of China (Grant No. 12571262), the 2025 Starlight Fund of Beijing Information Science and Technology University (Grant No. XG2025PT92), and the 2024 Project of the Beijing Higher Education Society (Grant No. MS2024378).

References

[1] Liu H D and Tian B 2026 *Appl. Math. Lett.* **172** 109688
[2] Onder I, Secer A, Ozisik M and Bayram M 2026 *Math. Methods Appl. Sci.* **49** 153
[3] Jia Y H, Wang D L, Shen B, Ju Z T, Huang Q Y, Wang X P, Zhang J H, Wang Y Y, Liu W and Dai C Q 2026 *Laser Photonics Rev.* **20** 2503212
[4] Jia Y H, Si Z Z, Ju Z T, Feng H Y, Zhang J H, Yan X and Dai C Q 2025 *Sci. China-Phys. Mech. Astron.* **68** 284211
[5] Zhou M X and Yu F J 2026 *Appl. Math. Lett.* **178** 109937
[6] Tian S F and Tong J F 2026 *Commun. Math. Phys.* **407** 52
[7] Liu J A, Li L, Yu F J and Liu M T 2026 *Phys. Scr.* **101** 155215
[8] Liu Y Q, Wen X Y and Wang D S 2019 *Comput. Math. Appl.* **77** 947
[9] Wu F, Liu Y Q and Yan Z Y 2025 *Physica D* **482** 134896
[10] Si Z Z, Ju Z T, Ren L F, Wang X P, Malomed B A and Dai C Q 2025 *Laser Photonics Rev.* **19** 2401019
[11] Liu Y Q, Guo B L and Wang D S 2026 *Acta Math. Appl. Sin. Engl. Ser.* **42** 582
[12] Xu S W, He J S and Wang L H 2011 *J. Phys. A* **44** 305203
[13] Aktosun T, Toledo I and Unlu M 2025 *Inverse Probl.* **41** 125008
[14] Ozawa T, Tian S F and Wu Z J 2026 *Math. Ann.* **394** 23
[15] Wu H Y 1995 *J. Math. Anal. Appl.* **192** 151
[16] Zhang J, Manafian J, Raut S, Roy S, Mahmoud K H and Alsubaie A S A 2024 *Nonlinear Dyn.* **112** 12375
[17] Yu J W and Yu F J 2026 *Appl. Math. Lett.* **174** 109827
[18] Wang X and Zhang Z H 2025 *Chin. Phys. B* **34** 090202
[19] Alam N, Akbar A, Ullah M S and Mostafa M 2025 *Indian J. Phys.* **99** 2125
[20] Akter M, Ulla M S, Wazwaz A M and Seadawy A R 2024 *Opt. Quant. Electron.* **56** 1127
[21] Ganie A H, Rahaman M S, Aladsani F A and Ullah M S 2025 *Nonlinear Dyn.* **113** 9807
[22] Gazizov R K and Ibragimov R H 1998 *Nonlinear Dyn.* **17** 387
[23] Yang J J, Tian S F and Li Z Q 2026 *Adv. Math.* **484** 110552
[24] Martin V D E and Peter W 2024 *J. Comput. Phys.* **514** 113167
[25] Lipnikov K, Manzini G and Shashkov M 2014 *J. Comput. Phys.* **257** 1163
[26] Binev P, Wolfgang D and Ron D 2004 *Numer. Math.* **97** 219
[27] Raissi M, Perdikaris P and Karniadakis G E 2019 *J. Comput. Phys.* **378** 686
[28] Chen Y Y, Lu L, Karniadakis G E and Negro L D 2020 *Opt. Express* **28** 11618
[29] Cai S Z, Mao Z P, Wang Z C, Yin M L and Karniadakis G E 2021 *Acta Mech. Sin.* **37** 1727
[30] Huang B and Wang J 2022 *IEEE Trans. Power Syst.* **38** 572
[31] Wang F J, Zhai Z, Zhao Z B, Di Y and Chen X F 2024 *Nat. Commun.* **15** 4332

[32] Pu J C, Li J and Chen Y 2021 *Nonlinear Dyn.* **105** 1723
[33] Han Y W, Zhuang J H, Li M C and Liu Y Q 2026 *Nonlinear Dyn.* **114** 25
[34] Yu J, Lu L, Meng X H and Karniadakis G E 2022 *Comput. Methods Appl. Mech. Engrg.* **393** 114823
[35] Yuan L, Ni Y Q, Deng X Y and Hao S 2022 *J. Comput. Phys.* **462** 111260
[36] Zhou H S, Zhang Z Y, Liu M W, Qi F H and Liu W J 2025 *Chin. Phys. Lett.* **42** 070001
[37] Pu J C and Chen Y 2024 *J. Comput. Phys.* **510** 113090
[38] Pu J C and Chen Y 2024 *Physica D* **467** 134262
[39] Kodama Y and Hasegawa A 1987 *IEEE J. Quantum Electron.* **23** 510
[40] Kim J, Park Q H and Shin H J 1998 *Phys. Rev. E* **58** 6746
[41] Li Y S and Han W T 2001 *Chin. Ann. Math. B* **22** 171
[42] Ankiewicz A, Soto-Crespo J M and Akhmediev N 2010 *Phys. Rev. E* **81** 046602
[43] Yang L, Meng X H and Karniadakis G E 2021 *J. Comput. Phys.* **425** 109913
[44] Jagtap A D, Kharazmi E and Karniadakis G E 2020 *Comput. Methods Appl. Mech. Engrg.* **365** 113028
[45] Rao C P, Sun H and Liu Y 2020 *Theory. Appl. Mech. Lett.* **10** 207
[46] Zhang R Y, Liu Y and Sun H 2020 *Comput. Methods Appl. Mech. Engrg.* **369** 113226
[47] Cuomo S, Di Cola V S, Giampaolo F, Rozza G, Raissi M and Piccialli F 2022 *J. Sci. Comput.* **92** 88
[48] Xiang Z X, Peng W, Liu X and Yao W 2022 *Neurocomputing* **496** 11
[49] Han J X, Xue L, Wei Y S, Qi Y D, Wang J L, Liu Y T and Zhang Y Q 2023 *Petrol. Sci.* **20** 3450
[50] Zhu C Y, Byrd R H, Lu P H and Nocedal J 1997 *ACM Trans. Math. Software* **23** 550
[51] Zhang C, Li L and Yu F J 2026 *Eur. Phys. J. Plus* **141** 544
[52] Chen J C, Chen L Y, Feng B F and Maruno K I 2019 *Phys. Rev. E* **100** 052216
[53] Tao Y S and He J S 2012 *Phys. Rev. E* **85** 026601
[54] Zhou Z J and Yan Z Y 2021 *Commun. Theor. Phys.* **73** 105006